Premelting, solid-fluid equlibria and thermodynamics in the high density region based on the Lennard-Jones potential

Andreas Köster,[1] Peter Mausbach,[2] and Jadran Vrabec[1, a)]

[1)] *Thermodynamics and Energy Technology, Universität Paderborn, 33098 Paderborn/Germany*

[2)] *Technical University of Cologne, 50678 Köln/Germany*

(Dated: 16 June 2017)

The Lennard-Jones potential is taken as a basis to study the high density fluid and fcc solid state region, including solid-fluid equilibria. Numerous thermodynamic property data are supplied, elucidating the behavior of matter in this poorly studied region. Particular attention is thereby paid to the premelting zone, a range of states close to the melting line, which is characterized by an accelerated variation of several thermodynamic properties. Because the underlying microscopic mechanisms are not yet fully understood, it is hoped that these data may contribute to the development of a theoretical framework for premelting effects. The present molecular simulation results are extensively compared to the latest and most accurate models for fluid and solid phases.

Keywords: Lennard-Jones, fluid and fcc solid state thermodynamics, premelting, equation of state, molecular simulation.

[a)]Corresponding author. E-mail address: jadran.vrabec@upb.de

I. INTRODUCTION

Thermodynamic states ranging from the high density fluid up to the solid have attracted a lot of interest in the past decade and a number of new theoretical approaches has been developed to discuss important aspects of this region[1–5]. However, this fact is accompanied by the surprising observation that closed thermodynamic information is available for hardly any real substance in this region. Common approaches to thermodynamic data are empirical equations of state (EOS). Unfortunately, there are only very few substances which were sufficiently measured in the laboratory to correlate high quality reference EOS[6]. A thermodynamic quantity which can serve as a measure for the quality of EOS correlations is the Grüneisen parameter γ_{G}, which was analyzed in detail in a recent paper on 28 real fluids[7]. That analysis showed that thermodynamic properties in the region beyond the triple point density are poorly described for most substances, mainly due to the lack of according experimental data.

The provision of complete thermodynamic information for a large region of the solid state is even more limited, a fact that should find more attention during the development of EOS that form the basis of common thermodynamic software tools[8–10]. The melting process is of particular interest for various practical applications. In contrast to the highly developed theory of melting in two dimensional (2D) systems, the more important premelting phenomena in three dimensional (3D) crystals are only inadequately understood. For these reasons, it is desirable to provide complete thermodynamic information at least for model substances in the region discussed above. The statistical mechanical formalism proposed by Lustig[11,12] allows for such an investigation because it incorporates, in principle, the calculation of an arbitrary number of partial Helmholtz energy derivatives in the canonic

(NVT) ensemble with a single simulation run. In the present study, we start developing this idea for the Lennard-Jones (LJ) potential.

The LJ interaction potential is widely used in molecular simulation studies because it is sufficiently realistic to represent small spherical and nonpolar molecules[13] and it is an important model for studying phase equilibria[14], phase change processes[15,16], clustering behavior[17], or transport[18] and interface properties[19] of simple fluids. For its fluid state, a number of high quality EOS can be found in the literature[20–24]. The LJ potential is commonly expressed as

$$u_{\mathrm{LJ}} = 4\varepsilon \left[\left(\frac{\sigma}{r}\right)^{12} - \left(\frac{\sigma}{r}\right)^{6} \right], \tag{1}$$

where σ and ε are its size and energy parameters, while r is the distance between two particles.

In this study, thermodynamic properties were investigated on the basis of Lustig's formalism[11,12] in a very large temperature and density range and, in this context, particular attention was paid to a detailed description of the premelting zone close to the melting line. For this purpose, solid-fluid equilibria (SFE) were determined up to high temperatures. Simulation results were compared to the latest and most accurate EOS in the fluid and solid phases. All numerical simulation data will be supplied in the supplementary material. The paper is organized as follows: Sections II and III introduce the molecular simulation method and the approach to determine SFE. Subsequently, the results of this study are discussed for the high density fluid (section IV) and solid state (section V). A conclusion sums the present findings up.

II. MOLECULAR SIMULATION METHOD

The molecular simulation tool $ms2$[25,26] was recently extended with the statistical mechanical formalism by Lustig[11,12], which allows for the concurrent sampling of an arbitrary number of partial Helmholtz energy derivatives in the canonic (NVT) ensemble during a single simulation run. Every time independent thermodynamic property can be calculated from a combination of these partial derivatives[6]. The total molar Helmholtz energy

$$a(T,\rho) = a^{\mathrm{o}}(T,\rho) + a^{\mathrm{r}}(T,\rho), \tag{2}$$

can be separated into an ideal (superscript "o") and a residual (superscript "r") contribution, where the latter is a consequence of the intermolecular interactions. For complex fluids, the ideal contribution to the Helmholtz energy is non-trivial and has to be determined experimentally (e.g. by spectroscopy) or by ab initio calculations. In the present case, the ideal contribution is straightforward because the LJ potential is monatomic. The reduced residual Helmholtz energy derivatives can be written as

$$A^{\mathrm{r}}_{mn} = (1/T)^m \rho^n \frac{\partial^{m+n} a^{\mathrm{r}}(T,\rho)/(RT)}{\partial(1/T)^m \partial\rho^n}, \tag{3}$$

wherein T denotes the temperature, ρ the density and R the ideal gas constant. m and n represent the order of the partial derivative with respect to density and inverse temperature, respectively. Although Lustig's formalism[11,12] may be used to sample the partial Helmholtz energy derivatives up to an arbitrary order, it was implemented in $ms2$ only up to the order of $m = 3$ and $n = 2$, yielding eight derivatives per simulation run. Table I gives an overview on their conversion into common thermodynamic properties. As usual for studies based on the LJ potential, all thermodynamic data are reported here in a reduced unit system. This

TABLE I. Thermodynamic properties in relation to the reduced Helmholtz energy derivatives, where the ideal contributions are $A^{\mathrm{o}}_{10} = -A^{\mathrm{o}}_{20} = 3/2$.

Property	Relation to the reduced Helmholtz energy derivatives
pressure $p = -(\partial a/\partial v)_T$	$\frac{p}{\rho RT} = 1 + A^{\mathrm{r}}_{01}$
internal energy $u = a - T(\partial a/\partial T)_v$	$\frac{u}{RT} = A^{\mathrm{o}}_{10} + A^{\mathrm{r}}_{10}$
enthalpy $h = u + pv$	$\frac{h}{RT} = 1 + A^{\mathrm{r}}_{01} + A^{\mathrm{o}}_{10} + A^{\mathrm{r}}_{10}$
isochoric heat capacity $c_v = (\partial u/\partial T)_v$	$\frac{c_v}{R} = -A^{\mathrm{o}}_{20} - A^{\mathrm{r}}_{20}$
isobaric heat capacity $c_p = (\partial h/\partial T)_p$	$\frac{c_p}{R} = -A^{\mathrm{o}}_{20} - A^{\mathrm{r}}_{20} + \frac{(1 + A^{\mathrm{r}}_{01} - A^{\mathrm{r}}_{11})^2}{1 + 2A^{\mathrm{r}}_{01} + A^{\mathrm{r}}_{02}}$
thermal expansion coefficient $\alpha = \frac{(\partial p/\partial T)_\rho}{\rho(\partial p/\partial \rho)_T}$	$\alpha T = \frac{1 + A^{\mathrm{r}}_{01} - A^{\mathrm{r}}_{11}}{1 + 2A^{\mathrm{r}}_{01} + A^{\mathrm{r}}_{02}}$
isothermal compressibilty $\beta_T = (\rho(\partial p/\partial \rho)_T)^{-1}$	$\beta_{\mathrm{T}}\rho RT = \frac{1}{1 + 2A^{\mathrm{r}}_{01} + A^{\mathrm{r}}_{02}}$
thermal pressure coefficient $\gamma_v = (\partial p/\partial \rho)_T$	$\frac{\gamma_v}{\rho} = 1 + A^{\mathrm{r}}_{01} - A^{\mathrm{r}}_{11}$
entropy gradient $(\partial s/\partial \rho)_T = 1/\rho^2(\partial^2 a/\partial T \partial v)$	$(\partial s/\partial \rho)_T \frac{\rho}{R} = -(1 + A^{\mathrm{r}}_{01} - A^{\mathrm{r}}_{11})$
density scaling exponent $\gamma = (\partial \ln T/\partial \ln \rho)_{s^{\mathrm{r}}}$	$\gamma R = -\frac{A^{\mathrm{r}}_{01} - A^{\mathrm{r}}_{11}}{A^{\mathrm{r}}_{20}}$
Grüneisen parameter $\gamma_G = \frac{(\partial p/\partial T)_\rho}{\rho c_v}$	$\gamma_G = -\frac{1 + A^{\mathrm{r}}_{01} - A^{\mathrm{r}}_{11}}{A^{\mathrm{o}}_{20} + A^{\mathrm{r}}_{20}}$
speed of sound $w = ((\partial p/\partial \rho)_s)^{1/2}$	$\frac{Mw^2}{RT} = 1 + 2A^{\mathrm{r}}_{01} + A^{\mathrm{r}}_{02} - \frac{(1 + A^{\mathrm{r}}_{01} - A^{\mathrm{r}}_{11})^2}{A^{\mathrm{o}}_{20} + A^{\mathrm{r}}_{20}}$
Joule-Thomson coefficient $\mu_{JT} = (\partial T/\partial p)_h$	$\mu_{\mathrm{JT}}\rho R = \frac{-(A^{\mathrm{r}}_{01} + A^{\mathrm{r}}_{02} + A^{\mathrm{r}}_{11})}{(1 + A^{\mathrm{r}}_{01} - A^{\mathrm{r}}_{11})^2 - (A^{\mathrm{o}}_{20} + A^{\mathrm{r}}_{20})(1 + 2A^{\mathrm{r}}_{01} + A^{\mathrm{r}}_{02})}$

reduction is based on the LJ size σ and energy ε parameters, e.g. $T^* = Tk_{\mathrm{B}}/\varepsilon$, $\rho^* = \rho\sigma^3$ and $p^* = p\sigma^3/\varepsilon$ with Boltzmann's constant k_{B} and pressure p. The asterisk in the superscript, however, will be omitted in the following.

Most simulations were carried out with $N = 1372$ particles using Monte Carlo (MC) sampling with an acceptance rate[27] of 0.5. Starting from a face centered cubic (fcc) lattice,

each run was equilibrated for 10^5 cycles and then sampled for 2 to $3 \cdot 10^6$ cycles, where one cycle corresponds to 1372 translational propagation attempts. The cutoff radius was chosen to be half of the edge length of the cubic simulation volume in the present simulations in order to evaluate the interactions explicitly to the largest possible extent. A detailed discussion of this choice is given in the appendix. Statistical uncertainties of the simulation data were estimated by block averaging[28] and the error propagation law was used for all subsequent calculations.

III. SOLID-FLUID EQUILIBRIA

For a study on the phase behavior of a thermodynamic system in the high density fluid region up to the solid state, solid-fluid coexistence plays a central role. Knowledge of the first-order freezing/melting transition is important in various fields, but it has proven to be difficult to give accurate predictions from experimental or theoretical treatments. Because key aspects of this phenomenon are poorly understood, computer simulation methods are valuable for exploring the freezing and melting behavior. For the LJ system, many results obtained from different calculation methods are available in the literature, such as the phase switch MC method[29,30], the interface pinning method[31], constrained λ - fluid integration[32] or Gibbs-Duhem integration (GDI)[33].

An alternative to these approaches, the so called GWTS algorithm, was introduced by Ge et al.[34] to determine the freezing point (FP) at a given temperature by applying small strain rates to the system using non-equilibrium molecular dynamics (MD) simulation. A change in the strain rate dependent pressure as a function of density indicates the presence of the FP. An entry into the two-phase fluid-solid region exhibits a sudden discontinuity of the zero strain rate pressure, whereas the pressure remains almost linear with increasing strain

rate[34,35]. Extending the isobaric tie line from the known FP to the solid state, calculated with equilibrium MD, then yields the melting point (MP). The GWTS algorithm has been successfully applied for the determination of solid-fluid coexistence of the Gaussian core[35], Weeks-Chandler-Andersen[36] and LJ potentials[37,38].

Ge et al.[34] mention that this phase transition can in principle also be determined by equilibrium MD or MC simulation without an applied strain. However, this approach requires small density increments to determine where exactly the pressure drop occurs on the liquid branch. This suggestion can naturally be combined with the thorough sampling of Helmholtz energy derivatives and because the present work is focused on thermodynamic data close to the freezing line (FL) and the melting line (ML), this approach was selected to determine the course of the FL and ML in (ρ, T) coordinates. The GWTS algorithm was applied along eight isotherms T = 1.3, 2, 3.5, 6, 10, 15, 22 and 30. Fig. 1 shows the density dependent equilibrium (zero strain) pressure at $T = 22$, indicating the pressure discontinuity at the FP density ρ_{FP} and the determination of the MP density ρ_{MP} as described above. The FP is at the end of the stable fluid branch and accordingly the MP is at the end of the stable solid branch. Metastable extensions of the fluid and solid state into the two-phase region are represented by dotted lines. Note that the metastable extension of the fluid branch was not determined in this study because metastable fluid state points of the SFE cannot be sampled straightforwardly by conventional MC. In the original version of the GWTS algorithm[34], the metastable extension of the fluid branch was determined by non-equilibrium MD simulations applying small, but finite strain rates to maintain the metastable state. The accuracy of the present method depends on the density increment $\Delta\rho$, which was set to 0.01 between adjacent simulation runs. Because of this discretization, slight scatter occurs between the coexistence points at different temperatures, which were,

however, averaged out by a fit procedure.

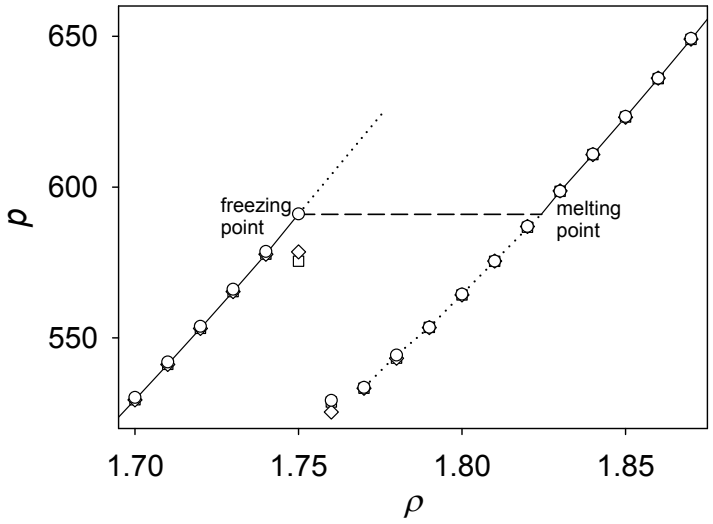

FIG. 1. Equilibrium (zero strain) pressure as a function of density at $T = 22$: (□) Present simulation data with parameter settings A, (◇) with parameter settings B, (○) with parameter settings C, (—) stable phase regions, $(\cdots)$ metastable extensions into the two-phase region (not sampled along the fluid branch). A detailed explanation of the parameter settings can be found in the appendix. The pressure discontinuity determines the freezing point density ρ_{FP} and the isobaric tie line to the solid branch yields the melting point density ρ_{MP}. Note that there are three symbols at every state point.

FP and MP coordinates generated in this way were used to fit a correlation function as employed by Ahmed and Sadus[37] and van der Hoef[39]

$$\rho_{\mathrm{FP}} = T^{1/4}[l_0 + l_1 T^{-1} + l_2 T^{-2} + l_3 T^{-3} + l_4 T^{-4} + l_5 T^{-5}] \,, \tag{4}$$

$$\rho_{\mathrm{MP}} = T^{1/4}[s_0 + s_1 T^{-1} + s_2 T^{-2} + s_3 T^{-3} + s_4 T^{-4} + s_5 T^{-5}] \,. \tag{5}$$

For a proper description of the FL and the ML in the vicinity of the triple point, additional FP and MP data in the temperature range $0.8 \leq T \leq 2.74$ from the literature[37] were considered in the present non-linear least square fitting procedure. The according empirical parameters l_i and s_i are summarized in Table II.

The resulting FL and ML, together with the present simulation results from the GWTS algorithm and those of Ahmed and Sadus[37], are shown in Fig. 2. Moreover, an extrapolation of the FL correlation from ref.[37] is also shown. Although only a limited temperature range $0.8 \leq T \leq 2.74$ was considered by Ahmed and Sadus[37], the agreement with the present results is satisfactory even at high temperatures. As shown by Thol et al.[24], an extrapolation of the ML based on the parameters given in ref.[37] fails numerically and is therefore omitted in Fig. 2. Ahmed and Sadus calculated SFE with the GDI algorithm[38], relying on initial conditions at $T = 2.74$ obtained with the GWTS algorithm. The associated FL and ML are also shown in Fig. 2. In a recent study, Heyes and Brańka[40] recalculated the course of the FL and the ML on the basis of molecular simulation data from the literature[30,38,41,42]. Their results closely follow the coexistence lines of Ahmed and Sadus[38] and are not shown in Fig. 2 for visibility reasons. It is striking that the coexistence lines from the GDI method deviate systematically from the results of the GWTS algorithm as the temperature increases, a result that was also noted by Sousa et al.[41]. Any error in the initial conditions of the GDI method, which differ in ref.[38] slightly from the published data based on the GWTS algorithm[37] at $T = 2.74$, will systematically propagate to all other temperatures. However, the majority of published SFE data are limited to a relatively small temperature interval. This region is shown in the inset of Fig. 2, where the results of Pedersen[31] are also depicted.

The entropy of fusion at the freezing/melting transition $\Delta s_{\text{fusion}} = \Delta h/T$, where Δh is the difference between the enthalpy of fluid and fcc crystal at the coexistence temperature T, is shown in Fig. 3. The entropy of fusion decreases rapidly with increasing temperature and approaches an almost constant value at higher temperatures. This behavior reflects the high degree of order of the solid phase at lower temperatures T compared to that at higher temperatures. At low temperatures, all simulation results are close to each other, at

TABLE II. Empirical parameters for the polynomial correlations (4) and (5) for the coexisting fluid and solid densities of the Lennard-Jones potential.

i	l_i	s_i
0	0.794644020380345	0.824314738009423
1	0.279493601324887	0.345860792558053
2	-0.368399926419796	-0.406050983191368
3	0.354753078269791	0.391153270627875
4	-0.167169591601731	-0.164344343309084
5	0.029246365939460	0.018024225929690

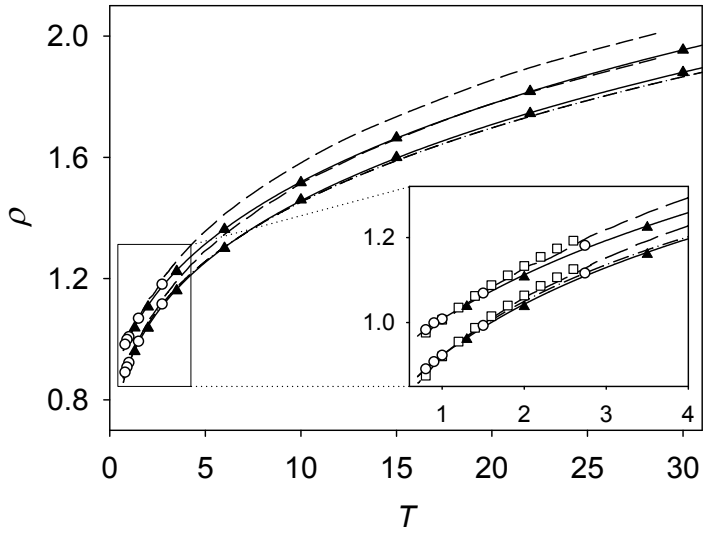

FIG. 2. Density ρ as a function of temperature along the freezing and the melting line: (▲) Present simulation data and (—) correlations thereof, cf. eqs. (4) and (5); (∘) Data of Ahmed and Sadus[37] and $(- \cdot -)$ an extrapolation of the freezing line correlation[37]; $(--)$ Coexistence data from the GDI algorithm[38]; (□) Data of Pedersen[31]. The freezing line is always below the melting line in this figure.

high temperatures, the data of Agrawal and Kofke[33] are above the present data. At $T \geq 6$, present values for Δs_{fusion} approach those of the solely repulsive r^{-12} potential for which $\Delta s_{\text{fusion}} = 0.9$[43].

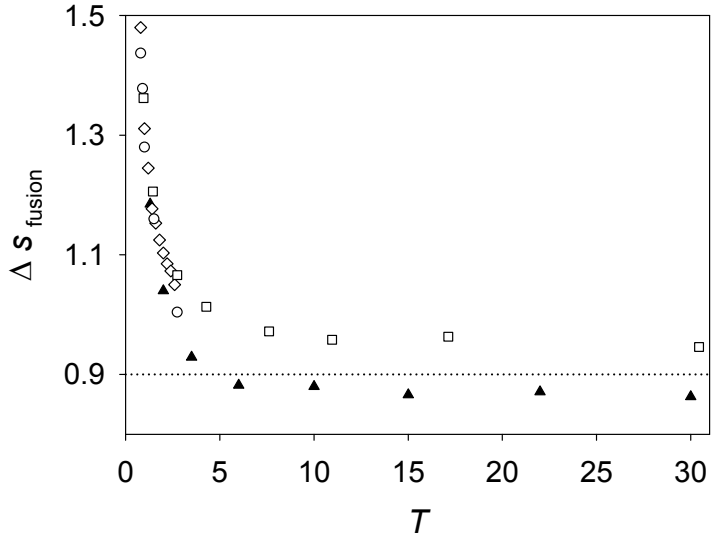

FIG. 3. Entropy of fusion Δs_{fusion} as a function of temperature: (▲) Present simulation data; (○) Data of Ahmed and Sadus[37]; (◇) Data of Pedersen[31]; (□) Data of Agrawal and Kofke[33]; $(\cdots)$ $\Delta s_{\text{fusion}} = 0.9$ in case of the r^{-12} potential[43].

The fractional density change at freezing $fdc = (\rho_{\text{MP}} - \rho_{\text{FP}})/\rho_{\text{FP}}$, also known as the miscibility gap, and the relative density difference at freezing $rdd = 2(\rho_{\text{MP}} - \rho_{\text{FP}})/(\rho_{\text{MP}} + \rho_{\text{FP}})$ are shown in Fig. 4. These two properties can be used to quantify the influence of the interaction potential on solid-fluid coexistence. Both fdc and rdd decrease significantly with increasing temperature, indicating that the two-phase region is narrower at high temperatures than at low temperatures. The fdc and rdd ratios of the r^{-12} potential are 0.038 and 0.037, respectively[43], cf. Fig. 4.

IV. THERMODYNAMIC PROPERTIES OF THE HIGH DENSITY FLUID STATE

Molecular simulation results ranging from the FL to the supercritical state of the LJ potential are presented along isochores in temperature dependent plots. The recently de-

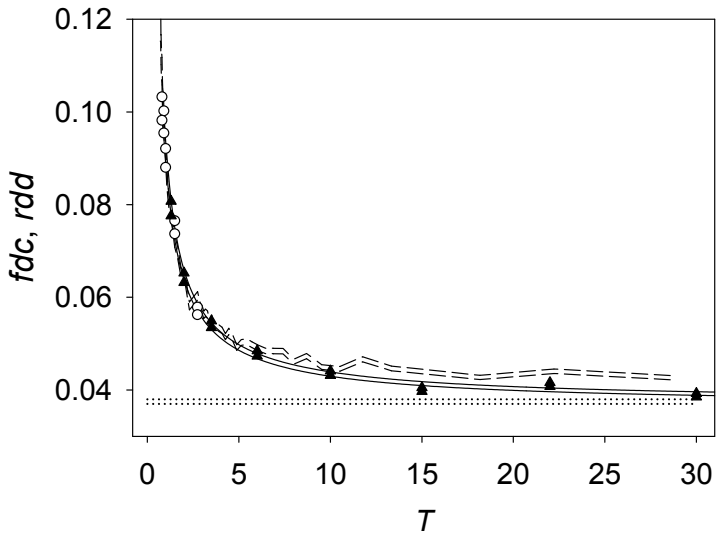

FIG. 4. Fractional density change at freezing fdc and relative density difference at freezing rdd as a function of temperature: (▲) Present simulation data and (—) correlations thereof, cf. eqs. (4) and (5); (∘) Data of Ahmed and Sadus[37]; (−−) Data of Ahmed and Sadus[38]; $(\cdots)$ fdc and rdd ratios corresponding to the r^{-12} potential[43]. The rdd curve is always below the fdc curve in this figure.

veloped reference EOS by Thol et al.[24] was used to assess the validity of the present data. Since the data set that was used by Thol et al.[24] for the parametrization of their EOS included state points in the range $0.7 < T < 9$ and $\rho < 1.08$, a large part of the present simulation data is compared to an extrapolation of that EOS. Thermodynamic properties on the FL itself can not be calculated from that EOS directly, instead (ρ, T) coordinates from the present FL correlation, cf. eq. (4), were employed to obtain those values. Note that statistical simulation uncertainties of the simulation data discussed in the following are only depicted, if they exceed symbol size.

A. First order derivative properties

Pressure p and enthalpy h are shown in Fig. 5. As expected, both the pressure p, which is displayed on a logarithmic scale, and the enthalpy h exhibit an almost linear increase with increasing temperature. The agreement with the EOS by Thol et al.[24] up to its specified limits is almost perfect, exhibiting relative deviations of 0.17 % for the pressure and 0.29 % for the enthalpy. At higher temperatures, somewhat larger deviations occur, especially along the FL and the $\rho = 1.4$ isochore.

B. Second order derivative properties

Second order derivative properties, i.e. isochoric heat capacity c_v, isobaric heat capacity c_p, thermal expansion coefficient α, isothermal compressibility β_T or thermal pressure coefficient γ_v, are relevant for a wide range of thermodynamic considerations.

Fig. 6 shows molecular simulation results for the isochoric and isobaric heat capacities, which decrease monotonically with increasing temperature in the homogeneous fluid state. Along the FL, however, c_v increases with temperature and seems to approach a constant value at very high temperatures. Deviations to the EOS by Thol et al.[24], especially for the four lowest isochores, are negligible. As expected, these deviations increase with both increasing temperature and density. The c_v and c_p data along the FL from the EOS by Thol et al.[24] and the present molecular simulations, however, agree only qualitatively. This discrepancy is most likely caused by the fact that the isochoric heat capacity c_v is a property which is very sensitive to phase transitions and therefore often serves as an equilibrium stability criterion, i.e. very small density variations in the vicinity of a coexistence curve lead to significant changes in terms of c_v[44,45]. Accordingly, the accuracy of the GWTS

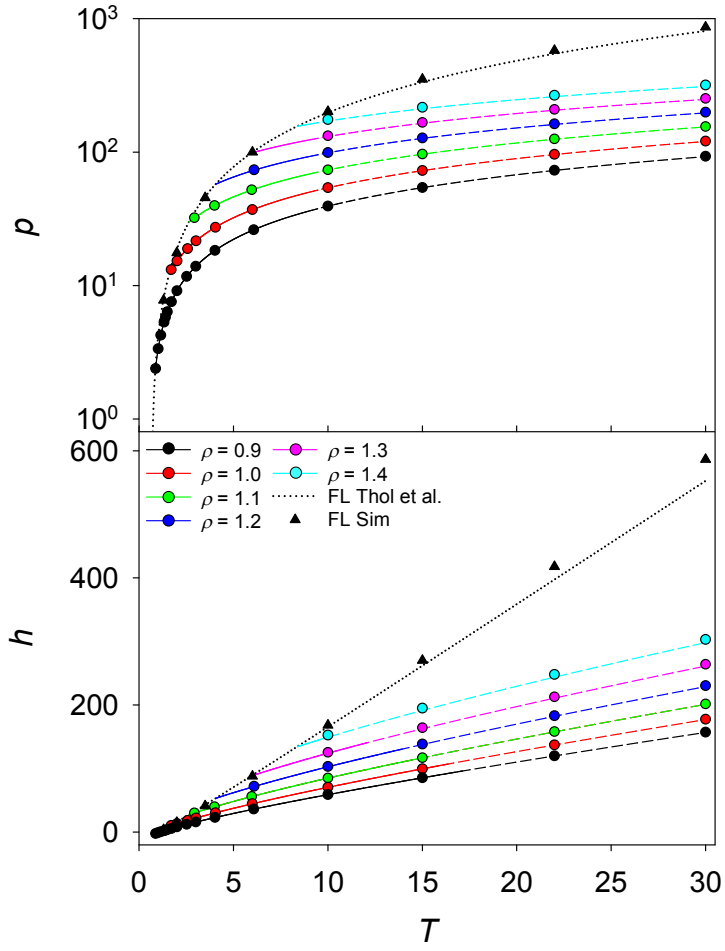

FIG. 5. Pressure p (top) and enthalpy h (bottom) along isochores in the high density fluid state: (—) EOS by Thol et al.[24], (−−) extrapolated and $(\cdots)$ using ρ and T coordinates from eq. (4) to calculate p and h values on the freezing line; (•) Present simulation data in the fluid phase and (▲) on the freezing line.

approach, which mainly depends on the density increment approaching the FL, strongly influences these data. Moreover, the density limit of the reference EOS by Thol et al.[24] is substantially exceeded on the FL, which seems to be particularly problematic for these thermodynamic properties.

The thermal expansion coefficient α and the isothermal compressibility β_T are depicted on a logarithmic scale in Fig. 7 (top and center). Both properties decrease monotonically

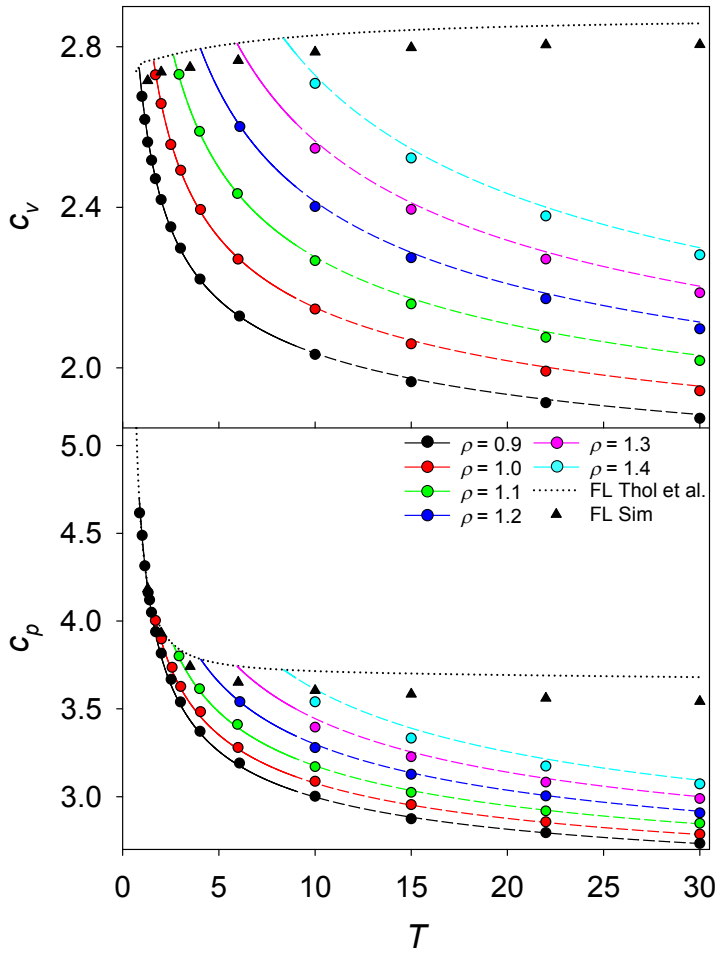

FIG. 6. Isochoric heat capacity c_v (top) and isobaric heat capacity c_p (bottom) along isochores in the high density fluid state: (—) EOS by Thol et al.[24], (−−) extrapolated and (···) using ρ and T coordinates from eq. (4) to calculate c_v and c_p values on the freezing line; (•) Present simulation data in the fluid phase and (▲) on the freezing line.

with increasing temperature. The density dependence of α is comparably smaller than that of β_T, whereas the temperature dependence is converse. A very good consistency between the EOS by Thol et al.[24] and the present molecular simulation data was found. Again, deviations are larger for very high densities and along the FL.

Fig. 7 (bottom) shows the thermal pressure coefficient γ_v, which is a combination of α

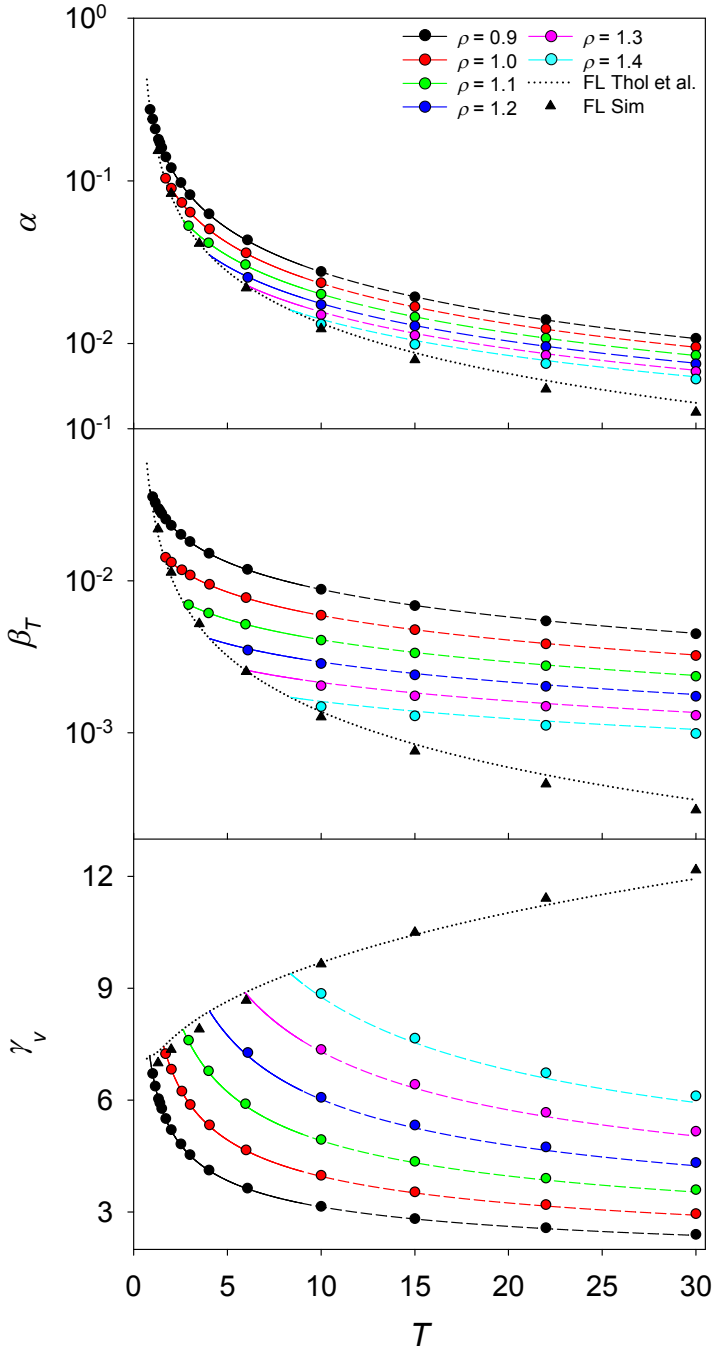

FIG. 7. Thermal expansion coefficient α, isothermal compressibility β_T and thermal pressure coefficient γ_v along isochores in the high density fluid state: (—) EOS by Thol et al.[24], (−−) extrapolated and (· · ·) using ρ and T coordinates from eq. (4) to calculate α, β_T and γ_v values on the freezing line; (•) Present simulation data in the fluid phase and (▲) on the freezing line.

and β_T. A good agreement between the present molecular simulation data and the EOS by Thol et al.[24] can be observed for $\rho \leq 1.2$, whereas deviations are larger for higher density. The molecular simulation results show a steeper slope along the FL than the EOS.

C. First and second order derivative properties

In this last section on the high density fluid region of the LJ potential, more complex and less popular thermodynamic properties are discussed. These are speed of sound w, Joule-Thomson coefficient μ_{JT}, Grüneisen parameter γ_G and density scaling exponent γ, cf. Figs. 8 and 9. The speed of sound w monotonically increases with increasing temperature. Beyond the range of validity of the EOS by Thol et al.[24], minor deviations to the present molecular simulation data were observed. At $\rho = 1.3$ and 1.4 as well as on the FL, an offset between the EOS and the molecular simulation data was found. Therefore, an extrapolation of the EOS by Thol et al.[24] with respect to the temperature seems to work reasonably well, whereas the density extrapolation less so.

Fig. 8 (center) depicts the Joule-Thomson coefficient. Both from molecular simulation and the EOS by Thol et al.[24] it can be seen that this property exhibits a minimum along the FL at low temperature. However, a constant offset between the molecular simulation data and the EOS by Thol et al.[24] was observed along that phase boundary. Upon an increase of temperature, each of the studied isochores tends towards a constant value. The agreement between the EOS by Thol et al.[24] and the molecular simulation data is satisfying for $\rho \leq 1.2$, while there are considerable deviations for $\rho = 1.3$ and 1.4. Note that the latter isochores are outside of the range of applicability of the EOS by Thol et al.[24].

The Grüneisen parameter monotonically decreases with increasing temperature, cf. Fig. 8 (bottom). A good agreement between the molecular simulation data and the EOS by Thol

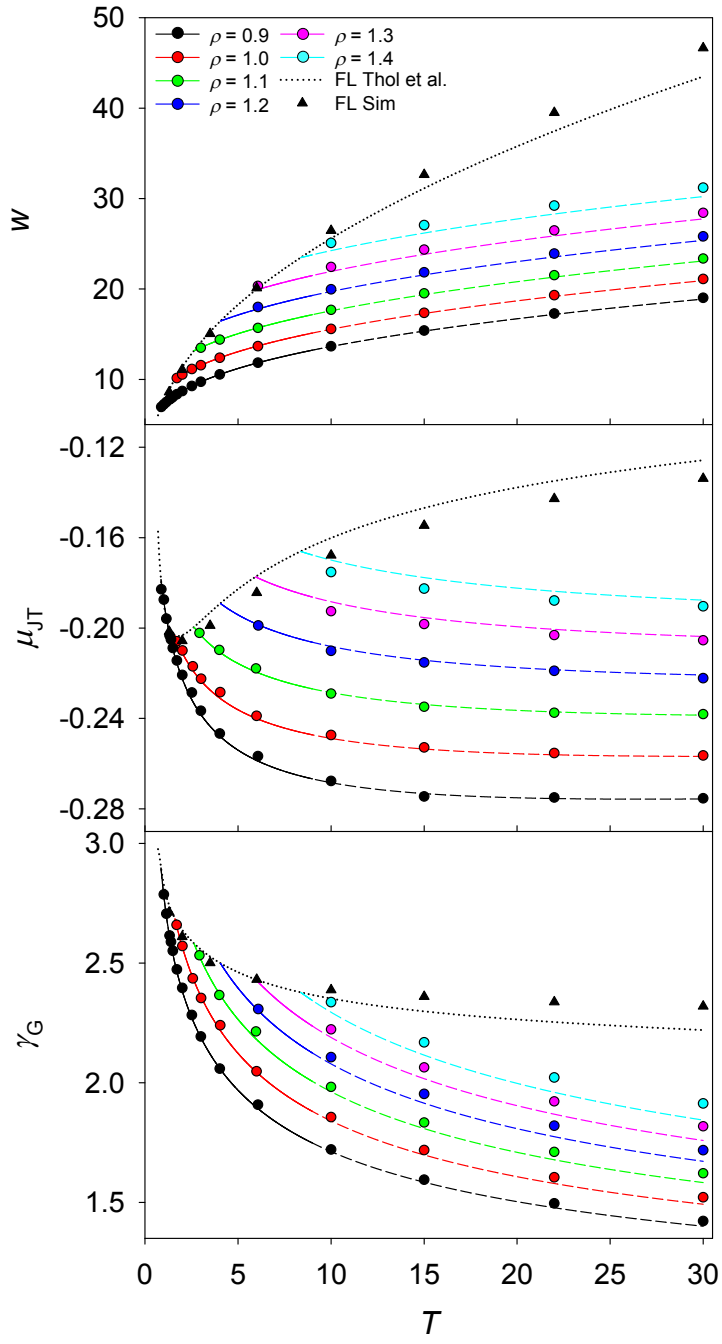

FIG. 8. Speed of sound w, Joule-Thomson coefficient $\mu_{\rm JT}$ and Grüneisen parameter γ_G along isochores in the high density fluid state: (—) EOS by Thol et al.[24], (−−) extrapolated and (· · ·) using ρ and T coordinates from eq. (4) to calculate w, $\mu_{\rm JT}$ and γ_G values on the freezing line; (•) Present simulation data in the fluid phase and (▲) on the freezing line.

et al.[24] was found for $T < 6$, at higher temperatures and higher densities deviations increase.

For the so called Roskilde simple systems (liquids and solids)[46–49], the existence of strong correlations between potential energy and virial fluctuations in the canonic (NVT) ensemble was recently identified and an isomorph theory[1] was developed to describe this class of systems. Isomorphs are curves of invariant structure and dynamics in the phase diagram. The LJ system exhibits strong virial-potential energy correlations when approaching the FL and it was proposed that the FL may be an isomorph[49]. A quantity which determines isomorphs in thermodynamic phase space is the density scaling exponent γ that can also be expressed in terms of Helmholtz energy derivatives, cf. Table I. Because of the central role of the density scaling exponent in isomorph theory, this property was studied as well.

Its temperature dependence along isochores is shown in Fig. 9 (top). The density scaling exponent γ decreases strongly for increasing temperature. Compared to all other properties, the largest deviations between the EOS by Thol et al.[24] and the present simulation results were observed for γ. These are most significant along the FL. For a comparison of γ along the FL, independent results from isomorph theory[50] were applied, cf. Fig. 9 (bottom). The correspondence between both calculation methods is very good in the entire density range. For very high density (and pressure) the density scaling exponent approaches a postulated value of $\gamma \approx 4$, which has to be expected only under extreme conditions[51]. This result shows that a severe extrapolation of the EOS by Thol et al.[24] beyond its defined scope can be problematic for certain properties.

V. THERMODYNAMIC PROPERTIES OF THE FCC SOLID STATE

Thermodynamic properties of the LJ solid as a fcc crystal obtained from simulation were compared with two solid state models that are given in terms of the Helmholtz energy. In

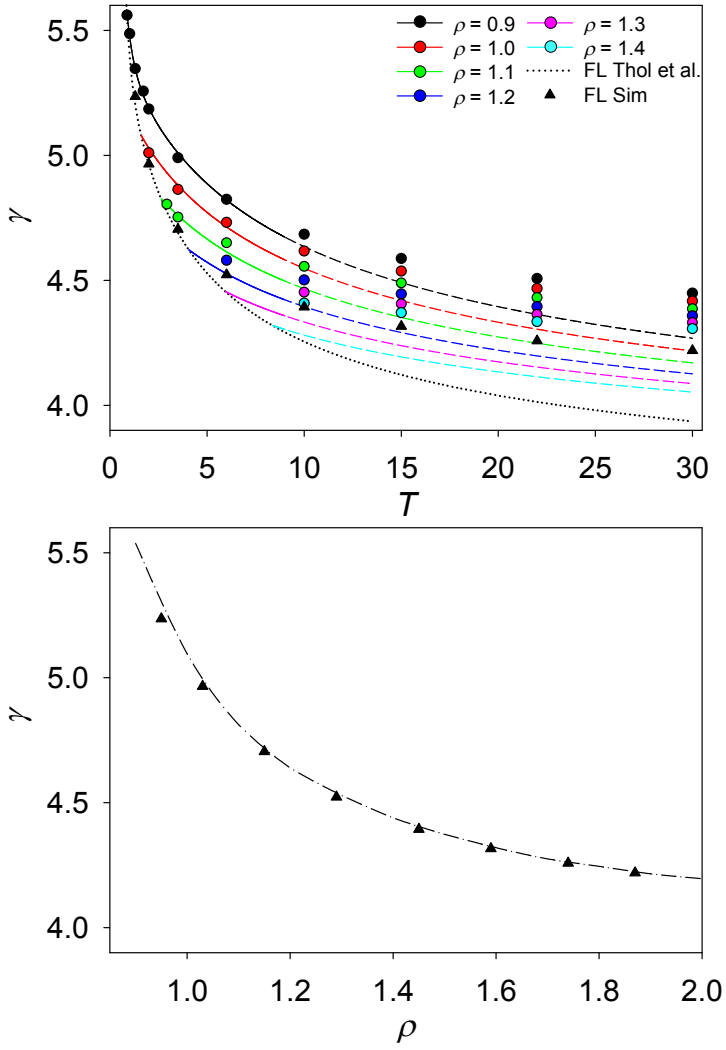

FIG. 9. Density scaling exponent γ along isochores in the high density fluid state (top) and on the FL (bottom): (—) EOS by Thol et al.[24], (−−) extrapolated and $(\cdots)$ using ρ and T coordinates from eq. (4) to calculate γ values on the freezing line; $(- \cdot -)$ Isomorph theory[50]; (•) Present simulation data in the fluid phase and (▲) on the freezing line.

contrast to models for the fluid phase, this type of equation for solids is rarely found in the literature. The most accurate EOS for the LJ fcc solid to date was published by van der Hoef[39,52], but it has a rather limited range of validity $0.1 \leq T \leq 2.0$ and $\rho_{m,s} \leq \rho \leq 1.2$, where $\rho_{m,s}$ is the density at melting or sublimation. A larger range of applicability is

provided by a very recent contribution of Lustig[53]. In his entirely theoretical approach, the Lennard-Jones and Devonshire (LJD) cell theory was developed to essentially obtain complete thermodynamic information for any cubic lattice, including fcc, and any interaction potential that is part of the Mie class[54].

A comparison of these three approaches is, in contrast to the fluid state, presented in density dependent plots along isotherms, which allows for a clearer depiction of the data. To better discern the presented thermodynamic data, some isotherms nonetheless had to be shifted to avoid overlaps. For a given thermodynamic quantity X, an offset was specified according to the following scheme

$$X_{shifted}(\rho, T_i) = X(\rho, T_i) + i\ \Delta_X\ , \tag{6}$$

with $i = 0, 1, 2, ..., 7$ and $T_0 = 1.3$, $T_1 = 2.0$, $T_2 = 3.5$,..., $T_7 = 30$. In the figures discussed in this section, simulation results from the fluid phase close to the FL are also shown for the isotherm $T = 1.3$. The behavior of the fluid branches of the other considered isotherms is similar to that of the isotherm $T = 1.3$ so that they were omitted for the sake of clarity. Furthermore, the presentation of simulation results was extended beyond the ML, covering the metastable solid in the two-phase region because superheated crystals are of significant interest[55,56]. Again, statistical uncertainties of the molecular simulation data are only shown in the plots, if they exceed symbol size.

A. First order derivative properties

Fig. 10 presents the pressure and the enthalpy, which are Helmholtz energy derivatives of first order. The coincidence between the EOS by van der Hoef[39], LJD theory[53] and present simulation results is very good. However, the enthalpy shows for low densities at T

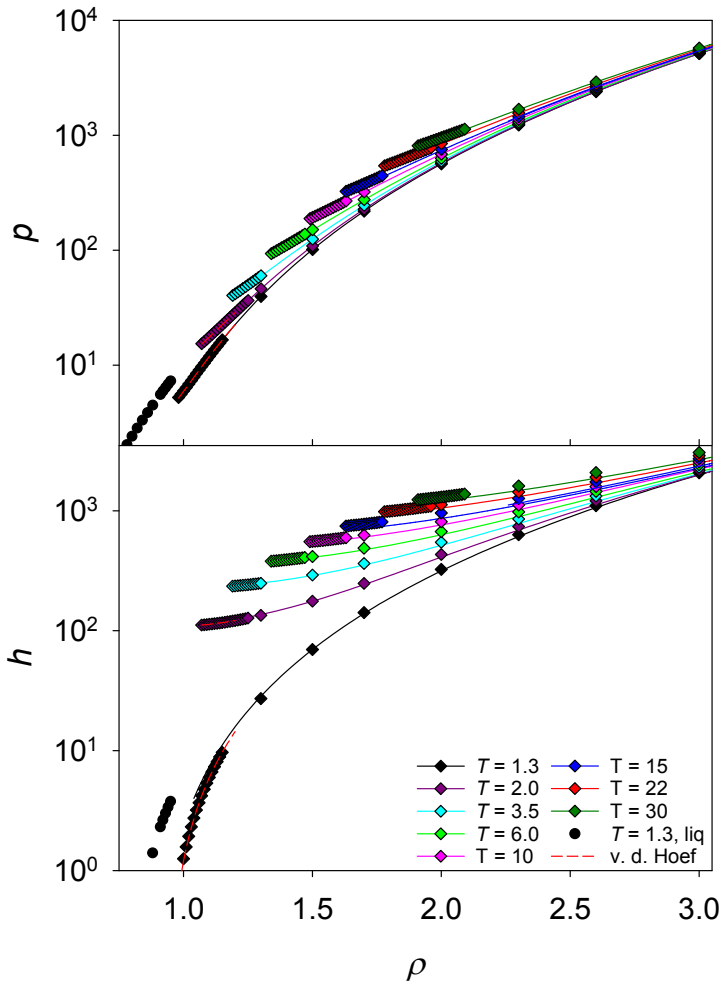

FIG. 10. Pressure p (top) and enthalpy h (bottom) of the fcc solid phase along different isotherms: (—) LJD theory[53]; (−−) EOS by van der Hoef[39]; (⧫) Present simulation data in the solid phase and (•) in the fluid phase at $T = 1.3$. Note the shift of the isotherms $\Delta_h = 100$ according to eq. (6).

= 1.3 a slightly better match between the EOS by van der Hoef[39] and the simulation data. Furthermore, the agreement of the enthalpy from LJD theory[53] and molecular simulation becomes slightly worse with increasing density and temperature. The pressure p was found to be roughly temperature independent for $\rho > 3$.

B. Heat capacities and premelting

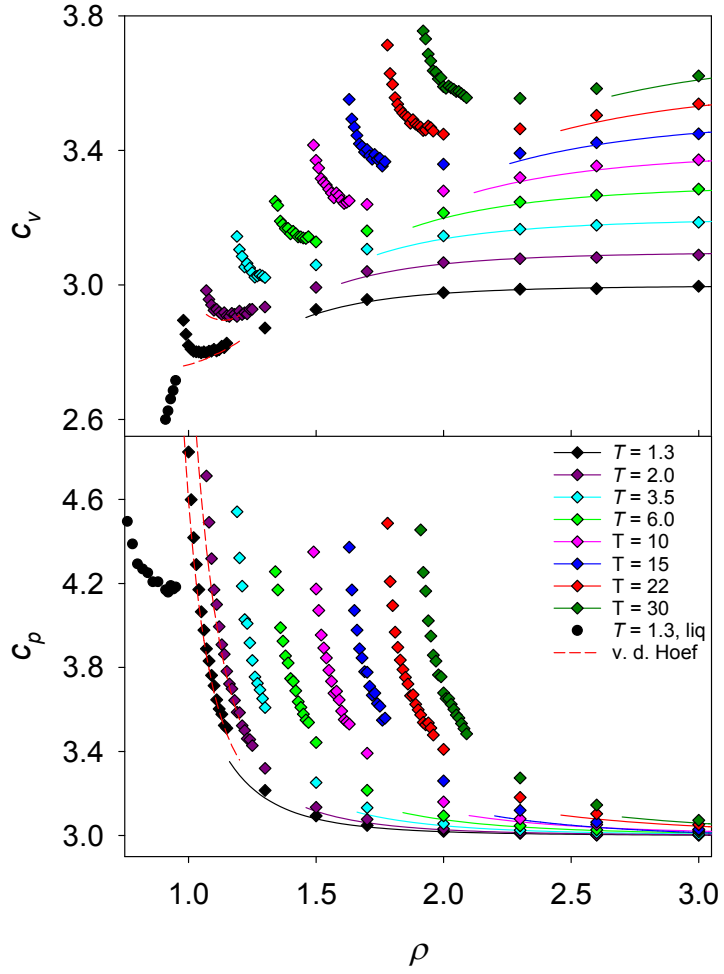

FIG. 11. Isochoric heat capacity c_v (top) and isobaric heat capacity c_p (bottom) of the fcc solid phase along different isotherms: (—) LJD theory[53]; (−−) EOS by van der Hoef[39]; (♦) Present simulation data in the solid phase and (•) in the fluid phase at $T = 1.3$. Note the shift of the isotherms $\Delta_{c_v} = 0.1$ according to eq. (6).

The isochoric heat capacity c_v is shown in Fig. 11 (top). An essentially perfect agreement between LJD theory[53] and the simulation data can be observed at higher densities, i.e. the relative deviation is only 0.1 % at $\rho = 3$. The results of both methods approach the well-known Dulong-Petit value of $c_v = 3$ at high densities. Reducing the density leads to a

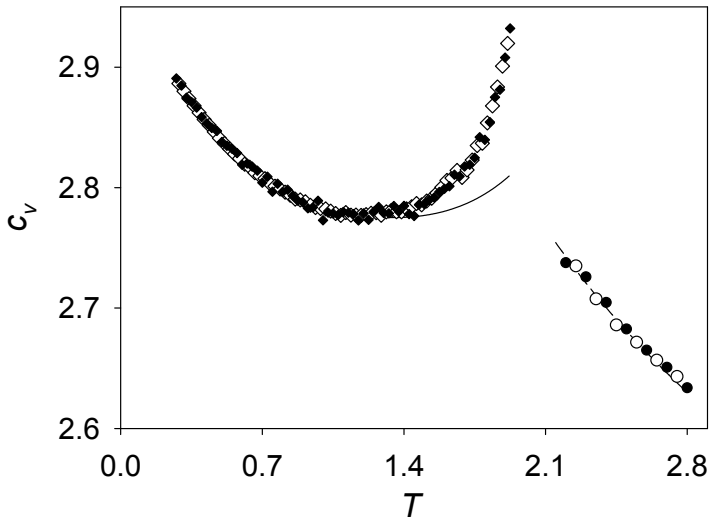

FIG. 12. Isochoric heat capacity c_v at $\rho = 1.05$ in the fluid and fcc solid phase: ($\blacklozenge$) Present molecular simulation data in the fcc solid phase obtained from A_{20} and ($\diamond$) obtained from $(\partial u/\partial T)_v$; ($\bullet$) Present simulation data in the fluid phase obtained from A_{20} and ($\circ$) obtained from $(\partial u/\partial T)_v$; (—) EOS by van der Hoef[39]; (−−) EOS by Thol et al.[24].

minimum of c_v along isotherms, followed by a sharp increase of the isochoric heat capacity upon approaching the ML. LJD theory[53] fails to reproduce this anomalous behavior of c_v. At least for $T = 2$, the EOS by van der Hoef[39] covers that anomaly reasonably well. However, it is useful to verify the anomalous behavior of c_v near the ML in more detail.

In this context, independently generated internal energy data u provide a severe test for the isochoric heat capacity c_v. Additional simulation runs were carried out along the isochore $\rho = 1.05$ to calculate c_v from the Helmholtz energy derivative A_{20} as well as its definition $c_v = (\partial u/\partial T)_v$. The derivative $(\partial u/\partial T)_v$ was approximated by the central difference quotient, filtering magnified noise with Savitzky-Golay smoothing[57]. Fig. 12 shows the results of both approaches. The agreement of the two simulation methods is very good and both data sets show a strong increase of c_v upon approaching the ML (at higher temperatures) and on the

other hand upon approaching the sublimation line (at lower temperatures). Agreement with the EOS by van der Hoef[39] is very good, only at higher temperatures the increase of c_v is not as pronounced as sampled by simulation. Both methods (using A_{20} or $(\partial u/\partial T)_v$) were also applied for the fluid phase and compared to the EOS by Thol et al.[24], cf. Fig. 12. The results show an excellent consistency.

The strong increase of c_v in the vicinity of the ML reflects a thermal response to bulk premelting effects, a long-standing, but still unsolved phenomenon in 3D crystals. Premelting can be thought of as a localized loss of crystalline order that can be observed well below the melting transition. Melting normally starts at an interface as a heterogeneous process. In contrast, homogeneous melting occurs in surface-free bulk crystals in which local failure of the crystalline phase arises due to defects in the equilibrium lattice structure. In molecular simulation, however, surface-free fcc crystals are typically maintained by periodic boundary conditions. It is well known that thermodynamic properties of solids experience accelerated variation in the vicinity of the ML due to lattice defects[58–60]. It is thus desirable to describe the according contributions concisely with a strict theoretical approach. However, a comprehensive theoretical framework that has been developed for 2D systems[61–63] could not be extended to 3D crystals so far. In 3D, the most reliable theories suggest that the defects breaking crystalline order are dislocation lines[55,64–68] that are emerging near the ML. Regardless of the fact that the microscopic mechanism of premelting is not fully understood, it is of interest to obtain quantitative information on the response behavior of thermodynamic properties due to these effects, which was one goal in this study.

The density dependent course of the isobaric heat capacity c_p is presented in Fig. 11 (bottom). A strong increase of c_p close to the ML was observed. The agreement between LJD theory[53] and simulation is good at high density, where the results again approach the

Dulong-Petit value of $c_p = 3$. The EOS by van der Hoef[39] agrees almost perfectly with the simulation data when approaching the ML. In contrast to c_v, the isobaric heat capacity does not exhibit a minimum along isotherms. Including the fluid region into the discussion, both heat capacities c_v and c_p exhibit along isotherms (Fig. 11) as well as isochores (Fig. 12) a λ-like shape when crossing the solid-fluid transition.

C. Isochoric heat capacity at low temperature

Two recent publications[69,70] investigated the low temperature phase diagram of the LJ solid. The authors determined the phase boundary between hexagonal closed packed (hcp) and fcc solids at very low, but finite temperatures. Both studies confirmed that the hcp solid is the equilibrium phase at low temperatures in a density range of $\rho_s < \rho \lesssim 2.1$, where ρ_s is the sublimation density, and that hcp-fcc coexistence exhibits reentrant behavior. It is thus of some interest to extend the calculations in this study also to low temperatures. Because the isochoric heat capacity c_v is sensitive to phase transitions, it was focused here on the behavior of c_v close to the postulated hcp-fcc transition[70].

To identify stable phase regions, Adidharma and Tan[70] calculated Helmholtz energy differences between the hcp and fcc solid phases of the LJ potential. For this purpose, residual internal energy u^{r} and pressure data in terms of the compressibility factor Z, obtained from simulation on hcp and fcc lattices, were correlated. In order to confirm the correct behavior of the present simulation data at low temperatures, they were compared to the data of Adidharma and Tan[70], cf. Fig. 13. The quantity u^{r}/T is presented along two isochores $\rho = 1.05$ and 1.3 as a function of temperature. For each isochore, all u^{r}/T values coincide. Because of their very close similarity, u^{r} of hcp and fcc solids differ only on the order of 10^{-3}. Deviations to the present simulation results are on the same order of magnitude,

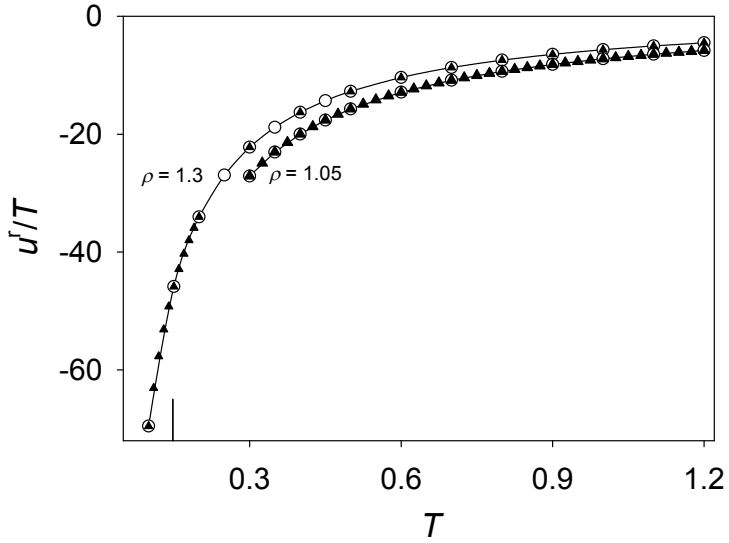

FIG. 13. Quotient of residual internal energy and temperature u^{r}/T along two isochores of $\rho = 1.05$ and 1.3 at low temperatures: (—) Fcc solid and (○) hcp solid from Adidharma and Tan[70]; (▲) Present simulation data in the fcc solid. The vertical bar at the lower temperature axis marks the postulated hcp-fcc solid-solid equilibrium at $\rho = 1.3$.

corroborating the present data at the hcp-fcc transition.

In Fig. 14, the isochoric heat capacity c_v is presented along two isochores. At $\rho = 1.3$, the outcome of all three approaches, i.e. molecular simulation, LJD theory[53] and an extrapolation of the EOS by van der Hoef[39], show in principle the same behavior, i.e. c_v decreases with increasing temperature. A remarkable variation of c_v at $\rho = 1.3$ in the vicinity of the hcp-fcc transition point was not observed, which is consistent with the findings of Fig. 13. At a density of $\rho = 3.0$, the simulated c_v data remain at the classical Dulong-Petit value of $c_v = 3$. The isochoric heat capacity obtained from the LJD theory[53], however, approaches zero for $T \to 0$. Note that the hcp phase disappears at $\rho = 3.0$[69].

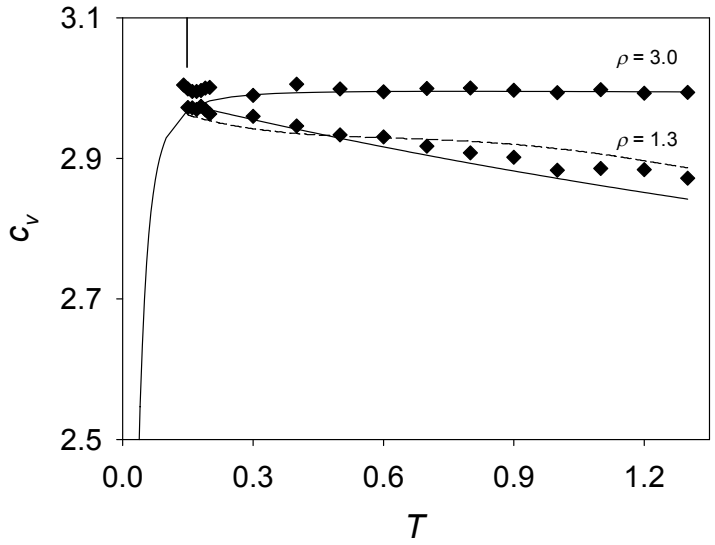

FIG. 14. Isochoric heat capacity c_v along two isochores of $\rho = 1.3$ and 3.0 at low temperatures: (—) Fcc solid from LJD theory[53]; (−−) Extrapolated EOS by van der Hoef[39]; (♦) Present simulation data in the fcc solid. The vertical bar at the upper temperature axis marks the postulated hcp-fcc solid-solid equilibrium at $\rho = 1.3$.

D. Other thermodynamic properties

The density dependent course of the thermal pressure coefficient γ_v is shown in Fig. 15 (top). Outside of the premelting zone, γ_v increases with increasing density. Close to the melting transition, the thermal pressure coefficient passes through a minimum and then rises at low temperatures, but not as pronounced as at higher temperatures.

Fig. 15 (center) shows the Joule-Thomson coefficient μ_{JT} along isotherms. The results obtained from the EOS by van der Hoef[39] agree very well with the present simulation data at low densities and temperatures, whereas LJD theory[53] agrees well at higher densities. A pronounced minimum occurs along all isotherms.

Isotherms of the Grüneisen parameter γ_G are presented in Fig. 15 (bottom), where simulated values exhibit only a very weak minimum at higher temperatures. γ_G depends

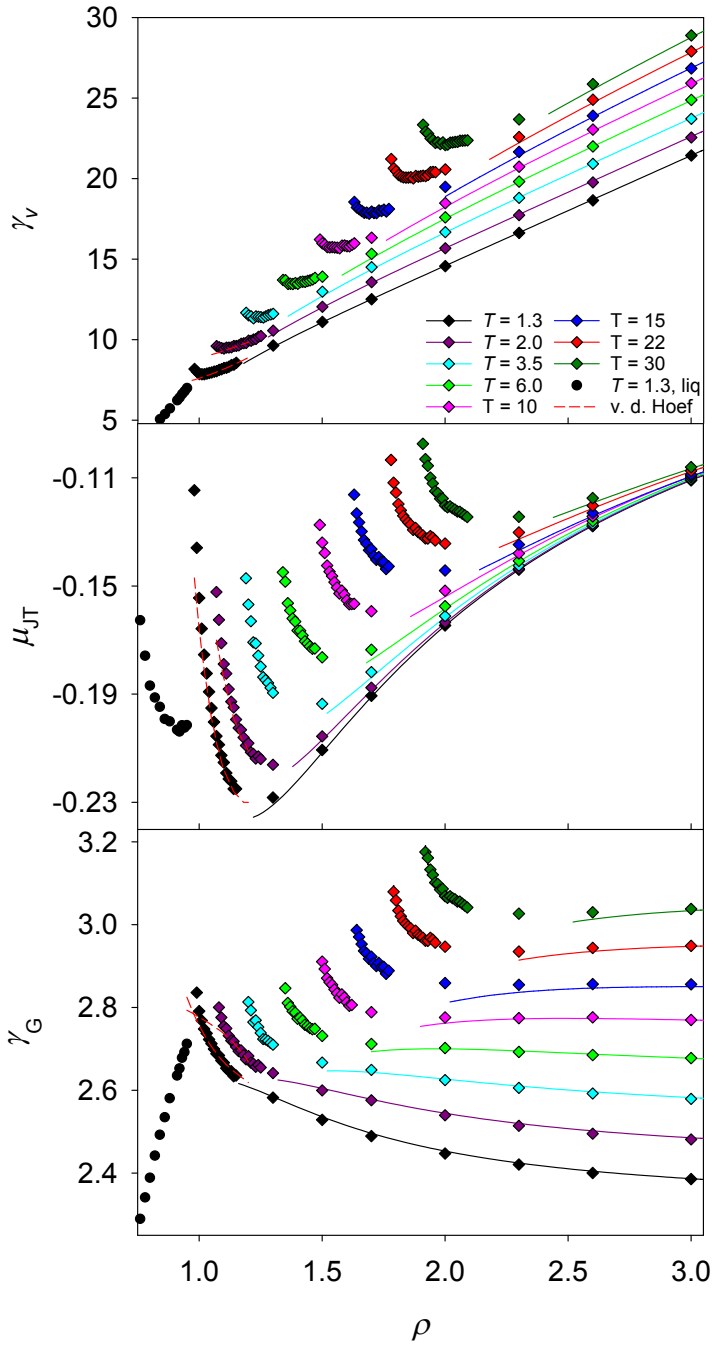

FIG. 15. Thermal pressure coefficient γ_v, Joule-Thomson coefficient $\mu_{\rm JT}$ and Grüneisen parameter γ_G of the fcc solid phase along different isotherms: (—) LJD theory[53]; (−−) EOS by van der Hoef[39]; (⧫) Present simulation data in the solid phase and (•) in the fluid phase at $T = 1.3$. Note the shift of the isotherms $\Delta_{\gamma_v} = 1.2$ and $\Delta_{\gamma_G} = 0.1$ according to eq. (6).

strongly on density and temperature in the premelting region, even a weak temperature dependence is present at high densities. Considering also the fluid data at $T = 1.3$, again a λ-like shape of γ_G around the solid-fluid transition was observed.

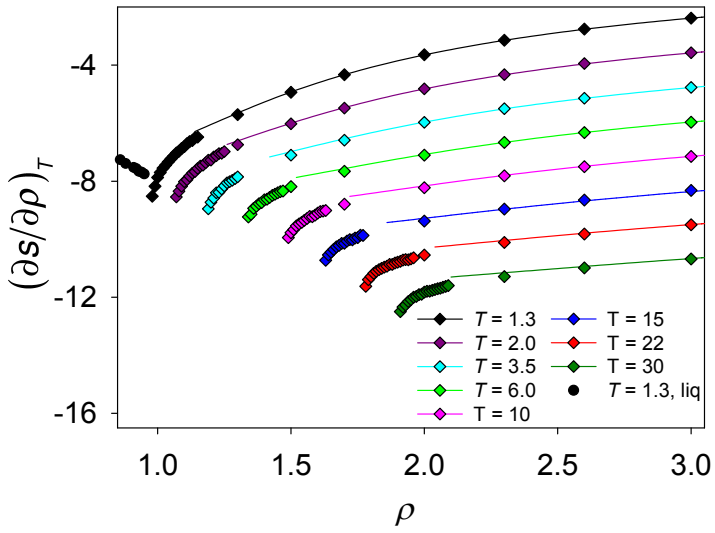

FIG. 16. Entropy derivative with respect to density at constant temperature $(\partial s/\partial \rho)_T$ of the fcc solid phase along different isotherms: (—) LJD theory[53]; (♦) Present simulation data in the solid phase and (•) in the fluid phase at $T = 1.3$. Note the shift of the isotherms $\Delta_{(\partial s/\partial \rho)_T} = -1.2$ according to eq. (6).

Premelting effects should also express themselves in the partial derivative of the entropy with respect to the density at constant temperature $(\partial s/\partial \rho)_T$, cf. Fig. 16. This derivative is negative, indicating that compression of the solid leads to a lower entropy s. The accelerating rate of $(\partial s/\partial \rho)_T$ close to the ML indicates more disorder caused by defects. Also in this case, LJD theory[53] does not reproduce the accelerated decrease of $(\partial s/\partial \rho)_T$.

Thermodynamic properties discussed so far exhibit good consistency between simulation data and LJD theory[53]. Both methods show an excellent agreement at higher densities. However, when approaching the ML, the simulation results show a more or less accelerated

variation, depending on the property considered, indicating a response to premelting effects. Thus LJD theory[53] obviously does not contain the underlying physics. Instead, the EOS by van der Hoef[39], as an equation correlated to simulation data, does describe the behavior of state properties in this region mostly with an acceptable accuracy, indicating proper extrapolation capability. However, there are thermodynamic properties for which LJD theory[53] much better predicts the phase behavior, at least qualitatively sometimes up to the ML. These state variables are reported in the remainder of this section.

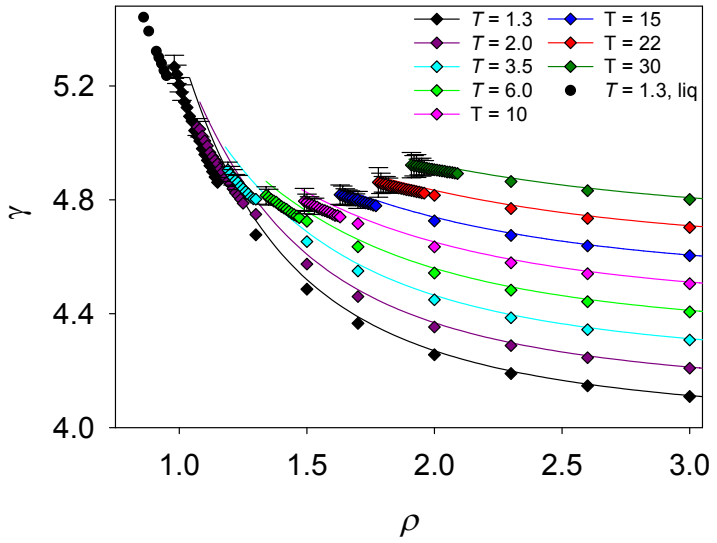

FIG. 17. Density scaling exponent γ of the fcc solid phase along different isotherms: (—) LJD theory[53]; (♦) Present simulation data in the solid phase and (•) in the fluid phase at $T = 1.3$. Statistical uncertainties are only displayed, if they exceed symbol size. Note the shift of the isotherms $\Delta_\gamma = 0.1$ according to eq. (6).

The density scaling exponent γ, as shown in Fig. 17, might be considered as a quantity in between these categories. γ from LJD theory[53] shows deviations with respect to simulation data in the vicinity of the ML, however, the qualitative behavior is predicted correctly. The density scaling exponent drops strongly with increasing density, approaching the postulated

value of $\gamma \approx 4.0$ at very high density (and pressure)[51].

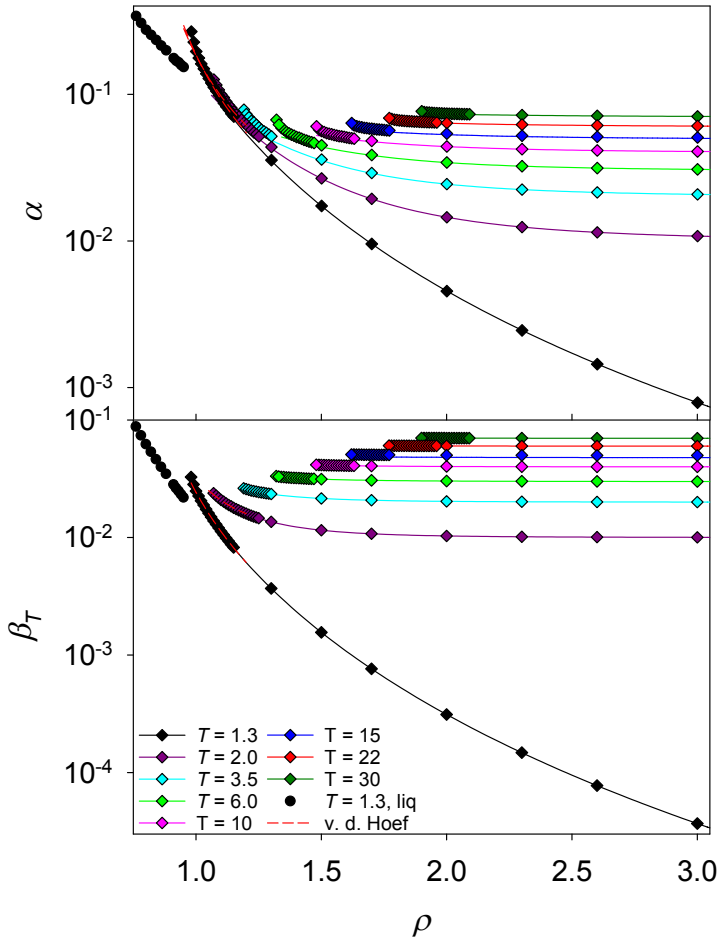

FIG. 18. Thermal expansion coefficient α and isothermal compressibility β_T of the fcc solid phase along different isotherms: (—) LJD theory[53]; (−−) EOS by van der Hoef[39]; (♦) Present simulation data in the solid phase and (•) in the fluid phase at $T = 1.3$. Note the shift of the isotherms $\Delta_\alpha = 0.01$ and $\Delta_{\beta_T} = 0.01$ according to eq. (6).

Fig. 18 (top) shows the thermal expansion coefficient α. Generally, α decreases very quickly with increasing density. Simulation data and LJD theory[53] agree very well for all densities and temperatures up to the ML, where only slight deviations between these approaches are observable. The EOS by van der Hoef[39] also coincides well with these calculations.

A similar situation was encountered for the isothermal compressibility β_T, as presented in Fig. 18 (bottom). All three calculation methods show a good agreement with each other. At high temperatures, only a weak density dependence was observed.

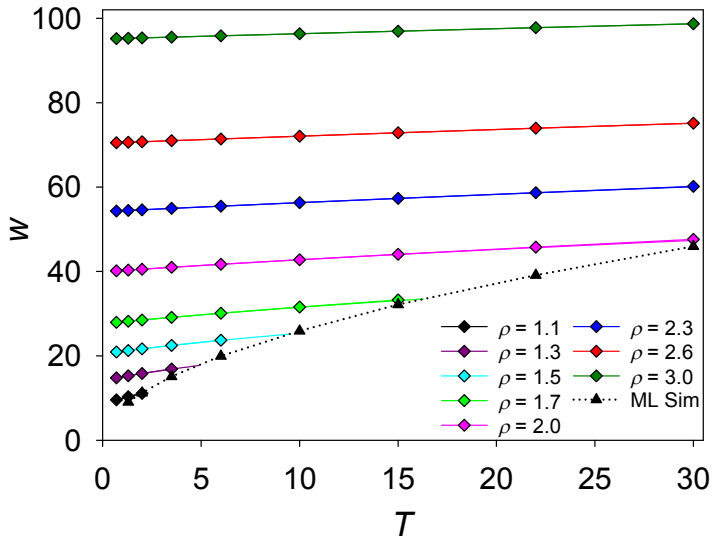

FIG. 19. Speed of sound w of the fcc solid phase along different isochores: (—) LJD theory[53]; (♦) Present simulation data in the solid phase and (▲) on the melting line calculated with the GWTS algorithm.

The speed of sound w is shown in Fig. 19. w depends strongly on density, but only weakly on temperature. Therefore, a temperature dependent representation along isochores was chosen to allow for a better overview. No remarkable premelting effects near the ML were found for the speed of sound. With an unsigned relative deviation of 0.06 %, the agreement between present simulation data and LJD theory[53] is almost perfect in the whole investigated phase space.

VI. CONCLUSION

Essentially complete thermodynamic information on time independent properties was determined for the LJ potential in a large range of states from the high density fluid up to the solid state. An entirely closed thermodynamic description of this state region, including the freezing/melting transition of first order, is rarely found in the literature. Molecular simulation results were compared to the latest and most accurate models for the fluid and solid phases. It was found that these equations lead, at least for some thermodynamic properties, to an inconsistent thermodynamic behavior close to the FL or the ML. Particular attention was paid to thermodynamics due to premelting effects near the ML. A theoretical framework describing premelting of 3D crystals has not been developed so far and simulations are a valuable tool for obtaining relevant information. It was shown that a number of properties exhibit accelerated variation in the premelting zone. Nevertheless, for the future, the question remains how these excitations can be described and how a connection to the underlying microscopic mechanisms can be developed. A promising path might be the one recently proposed by Köbler and Bodryakov[71], describing heat capacity data by means of critical-like power functions.

Acknowledgments

The authors thank Rolf Lustig for providing a computer program to calculate different properties within the framework of his LJD theory[53] as well as for valuable advice and fruitful discussions. Furthermore, the authors gratefully acknowledge the Paderborn Center for Parallel Computing (PC^2) for the generous allocation of computer time on the OCuLUS cluster and computational support by the High Performance Computing Center Stuttgart

(HLRS) under the grant MMHBF2. The present research was conducted under the auspices of the Boltzmann-Zuse Society of Computational Molecular Engineering (BZS).

APPENDIX

A. Parameter setting analysis

It is useful to compare the influence of different simulation parameters on the sampled thermodynamic properties of the LJ system. For this purpose, default parameter settings introduced in section II (parameter settings A) were varied. Investigating SFE may, e.g., be sensitive to potential cutoff conditions and system size. Therefore, separate simulations were performed at $T = 22$ to analyze the dependence of the simulation results on the cutoff conditions (parameter settings B) and on the particle number (parameter settings C).

Parameter settings B were the same as parameter settings A with a sufficiently large, but constant cutoff radius ($r_c = 4\sigma$). For parameter settings C, the number of particles was set to $N = 4000$, whereas all other parameters remained the same as for parameter settings A. The results of these two additional series are presented in Fig. 1, exhibiting almost the same behavior as for parameter settings A. These findings confirm results for rare-gas crystals from MC simulations with the LJ potential[72]. Bocchetti and Diep[72] determined the melting temperature for different system sizes, showing that the melting temperature does not significantly depend on system size for particle numbers $N \geq 500$. The maximum relative deviation between parameter settings A and B was below 0.05% and between parameter settings A and C below 0.15%.

Similar to the investigation of the pressure in Fig. 1, all other thermodynamic properties considered in this study were also analyzed for a dependence on simulation parameters along

the isotherm $T = 22$. For a thermodynamic quantity X, the relative difference according to $100\,(X_A - X_i)/X_A$ was calculated. The differences between parameter settings A and B and the differences between parameter settings A and C were calculated.

The largest maximum difference between the employed parameter settings was found for the isobaric heat capacity c_p with 1.4 % for parameter settings B and 3 % for parameter settings C relative to parameter settings A. The maximum differences are summarized in Table III for all other thermodynamic properties. The application of parameter settings C yields larger relative differences with respect to parameter settings A. However, considering that these values are the maximum deviations and that higher thermodynamic derivatives are more challenging to calculate or to measure in general, the results are very satisfactory. For this reason, we applied exclusively parameter settings A to sample the molecular simulation results discussed above.

TABLE III. Maximum relative deviations of different thermodynamic properties calculated with parameter settings B and parameter settings C parameters relative to parameter settings A at the temperature $T = 22$.

Property		Parameter settings B [%]	Parameter settings C [%]
pressure	p	0.05	0.15
enthalpy	h	0.04	0.14
isochoric heat capacity	c_v	1.0	1.6
isobaric heat capacity	c_p	1.4	3.0
speed of sound	w	0.04	0.15
Grüneisen parameter	γ_G	0.5	1.25
density scaling exponent	γ	0.04	0.12
thermal pressure coefficient	γ_V	1.2	3.0
isothermal compressibilty	β_T	0.7	1.5
thermal expansion coefficient	α	2	4.4
entropy gradient	$(\partial s/\partial \rho)_T$	1.2	3.0

REFERENCES

[1]J. C. Dyre, J. Phys. Chem. B **118**, 10007 (2014).

[2]D. Fragiadakis and C. M. Roland, Phys. Rev. E **83**, 031504 (2011).

[3]D. Bolmatov, V. V. Brazhkin, and K. Trachenko, Nat. Commun. **4**, 2331 (2013).

[4]Y. Rosenfeld and P. Tarazona, Mol. Phys. **95**, 141 (1998).

[5]G. Ruppeiner, P. Mausbach, and H.-O. May, Phys. Lett. A **379**, 646 (2015).

[6]R. Span, *Multiparameter Equations of State: An Accurate Source of Thermodynamic Property Data* (Springer Verlag, Berlin, 2000).

[7]P. Mausbach, A. Köster, G. Rutkai, M. Thol, and J. Vrabec, J. Chem. Phys. **144**, 244505 (2016).

[8]R. Span, T. Eckermann, S. Herrig, S. Hielscher, A. Jäger, and M. Thol, "TREND. Thermodynamic Reference and Engineering Data 3.0," Lehrstuhl für Thermodynamik, Ruhr-Universität Bochum, Germany (2016).

[9]E. W. Lemmon, M. L. Huber, and M. O. McLinden, "NIST reference fluid thermodynamic and transport properties–REFPROP," NIST Standard Reference Database 23, v9.1 (2002).

[10]I. H. Bell, J. Wronski, S. Quoilin, and V. Lemort, Ind. Eng. Chem. Res. **53**, 2498 (2014).

[11]R. Lustig, Mol. Sim. **37**, 457 (2011).

[12]R. Lustig, Mol. Phys. **110**, 3041 (2012).

[13]G. Rutkai, M. Thol, R. Span, and J. Vrabec, Mol. Phys. **115**, 1104 (2016).

[14]A. Lotfi, J. Vrabec, and J. Fischer, Mol. Phys. **76**, 1319 (1992).

[15]M. Heinen, J. Vrabec, and J. Fischer, J. Chem. Phys. **145**, 081101 (2016).

[16]M. Horsch, J. Vrabec, and H. Hasse, Phys. Rev. E **78**, 011603 (2008).

[17]M. Horsch, J. Vrabec, M. Bernreuther, S. Grottel, G. Reina, A. Wix, K. Schaber, and H. Hasse, J. Chem. Phys. **128**, 164510 (2008).

[18]G. A. Fernandez, J. Vrabec, and H. Hasse, Fluid Phase Equilib. **221**, 157 (2004).

[19]J. Vrabec, G. K. Kedia, G. Fuchs, and H. Hasse, Mol. Phys. **104**, 1509 (2006).

[20]J. K. Johnson, J. A. Zollweg, and K. E. Gubbins, Mol. Phys. **78**, 591 (1993).

[21]J. Kolafa and I. Nezbeda, Fluid Phase Equilib. **100**, 1 (1994).

[22]M. Mecke, A. Müller, J. Winkelmann, J. Vrabec, J. Fischer, R. Span, and W. Wagner, Int. J. Thermophys. **17**, 391 (1996), Erratum **19**, 1493 (1998).

[23]H.-O. May and P. Mausbach, Phys. Rev. E **85**, 031201 (2012), Erratum **86**, 059905 (2012).

[24]M. Thol, G. Rutkai, A. Köster, R. Lustig, R. Span, and J. Vrabec, J. Phys. Chem. Ref. Data **45**, 023101 (2016).

[25]S. Deublein, B. Eckl, J. Stoll, S. V. Lishchuk, G. Guevara-Carrion, C. W. Glass, T. Merker, M. Bernreuther, H. Hasse, and J. Vrabec, Comput. Phys. Commun. **182**, 2350 (2011).

[26]C. W. Glass, S. Reiser, G. Rutkai, S. Deublein, A. Köster, G. Guevara-Carrion, A. Wafai, M. Horsch, M. Bernreuther, T. Windmann, H. Hasse, and J. Vrabec, Comput. Phys. Commun. **185**, 3302 (2014).

[27]D. Frenkel and B. Smit, *Understanding Molecular Simulation: From Algorithms to Applications* (Elsevier, San Diego, 2001).

[28]H. Flyvbjerg and H. G. Petersen, J. Chem. Phys. **91**, 461 (1989).

[29]J. R. Errington, J. Chem. Phys. **120**, 3130 (2004).

[30]G. C. McNeil-Watson and N. B. Wilding, J. Chem. Phys. **124**, 064504 (2006).

[31]U. R. Pedersen, J. Chem. Phys. **139**, 174502 (2013).

[32]G. Grochola, J. Chem. Phys. **120**, 2122 (2004).

[33]R. Agrawal and D. A. Kofke, Mol. Phys. **85**, 43 (1995).

[34]J. Ge, G.-W. Wu, B. Todd, and R. J. Sadus, J. Chem. Phys. **119**, 11017 (2003).

[35]P. Mausbach, A. Ahmed, and R. J. Sadus, J. Chem. Phys. **131**, 184507 (2009), Erratum **132**, 019901 (2010).

[36]A. Ahmed and R. J. Sadus, Phys. Rev. E **80**, 061101 (2009).

[37]A. Ahmed and R. J. Sadus, J. Chem. Phys. **131**, 174504 (2009), Erratum **133**, 229902 (2010).

[38]A. Ahmed and R. J. Sadus, J. Chem. Phys. **133**, 124515 (2010).

[39]M. A. Van der Hoef, J. Chem. Phys. **113**, 8142 (2000).

[40]D. Heyes and A. Brańka, J. Chem. Phys. **143**, 234504 (2015).

[41]J. Sousa, A. Ferreira, and M. Barroso, J. Chem. Phys. **136**, 174502 (2012).

[42]E. A. Mastny and J. J. de Pablo, J. Chem. Phys. **127**, 104504 (2007).

[43]W. G. Hoover, S. G. Gray, and K. W. Johnson, J. Chem. Phys. **55**, 1128 (1971).

[44]V. Baidakov, S. Protsenko, and Z. Kozlova, Chem. Phys. Lett. **447**, 236 (2007).

[45]V. Baidakov, S. Protsenko, and Z. Kozlova, Fluid Phase Equilib. **263**, 55 (2008).

[46]N. P. Bailey, U. R. Pedersen, N. Gnan, T. B. Schrøder, and J. C. Dyre, J. Chem. Phys. **129**, 184507 (2008).

[47]N. P. Bailey, U. R. Pedersen, N. Gnan, T. B. Schrøder, and J. C. Dyre, J. Chem. Phys. **129**, 184508 (2008).

[48]T. B. Schrøder, N. P. Bailey, U. R. Pedersen, N. Gnan, and J. C. Dyre, J. Chem. Phys. **131**, 234503 (2009).

[49]N. Gnan, T. B. Schrøder, U. R. Pedersen, N. P. Bailey, and J. C. Dyre, J. Chem. Phys. **131**, 234504 (2009).

[50]L. Costigliola, T. B. Schrøder, and J. C. Dyre, Phys. Chem. Chem. Phys. **18**, 14678 (2016).

[51]U. R. Pedersen, N. P. Bailey, T. B. Schrøder, and J. C. Dyre, Phys. Rev. Lett. **100**, 015701 (2008).

[52]M. A. van der Hoef, J. Chem. Phys. **117**, 5092 (2002).

[53]R. Lustig, Mol. Phys. **115**, 1362 (2017).

[54]G. Mie, Ann. Phys. **316**, 657 (1903).

[55]L. Gómez, C. Gazza, H. Dacharry, L. Peñaranda, and A. Dobry, Phys. Rev. B **71**, 134106 (2005).

[56]A. Belonoshko, S. Davis, N. V. Skorodumova, P.-H. Lundow, A. Rosengren, and B. Johansson, Phys. Rev. B **76**, 064121 (2007).

[57]A. Savitzky and M. J. E. Golay, Anal. Chem. **36**, 1627 (1964).

[58]W. D. Kristensen, E. Jensen, and R. Cotterill, Philos. Mag. **30**, 229 (1974).

[59]R. Crawford, W. Lewis, and W. Daniels, J. Phys. C: Solid State Phys. **9**, 1381 (1976).

[60]V. Y. Bodryakov, Tech. Phys. **58**, 722 (2013).

[61]J. M. Kosterlitz and D. J. Thouless, J. Phys. C: Solid State Phys. **6**, 1181 (1973).

[62]D. R. Nelson and B. Halperin, Phys. Rev. B **19**, 2457 (1979).

[63]A. Young, Phys. Rev. B **19**, 1855 (1979).

[64]H. Kleinert, *Gauge theory in condensed matter* (World Scientific, Singapore, 1989).

[65]L. Burakovsky, D. L. Preston, and R. R. Silbar, Phys. Rev. B **61**, 15011 (2000).

[66]L. Gómez, A. Dobry, and H. Diep, Phys. Rev. B **63**, 224103 (2001).

[67]L. Gómez, A. Dobry, C. Geuting, H. Diep, and L. Burakovsky, Phys. Rev. Lett. **90**, 095701 (2003).

[68]A. M. Alsayed, M. F. Islam, J. Zhang, P. J. Collings, and A. G. Yodh, Science **309**, 1207 (2005).

[69]C. Calero, C. Knorowski, and A. Travesset, J. Chem. Phys. **144**, 124102 (2016).

[70]H. Adidharma and S. P. Tan, J. Chem. Phys. **145**, 014503 (2016).

[71]U. Köbler and V. Bodryakov, Int. J. Thermodyn. **18**, 200 (2015).

[72]V. Bocchetti and H. T. Diep, J. Chem. Phys. **138**, 104122 (2013).